A discrete dislocation analysis of mode I crack growth

Cleveringa, H.H.M.; van der Giessen, E.; Needleman, A.

Published in:
Journal of the Mechanics and Physics of Solids

DOI:
10.1016/S0022-5096(99)00076-9

Publication date:
2000


PERGAMON

Journal of the Mechanics and Physics of Solids
48 (2000) 1133–1157

JOURNAL OF THE
MECHANICS AND
PHYSICS OF SOLIDS

www.elsevier.com/locate/jmps

A discrete dislocation analysis of mode I crack growth

H.H.M. Cleveringa[a], E. Van der Giessen[a], A. Needleman[b,*]

[a]*Delft University of Technology, Koiter Institute Delft, Mekelweg 2, 2628 CD Delft, The Netherlands*
[b]*Brown University, Division of Engineering, Providence, RI 02912, USA*

Received 22 February 1999; received in revised form 5 July 1999

Abstract

Small scale yielding around a plane strain mode I crack is analyzed using discrete dislocation dynamics. The dislocations are all of edge character, and are modeled as line singularities in an elastic material. At each stage of loading, superposition is used to represent the solution in terms of solutions for edge dislocations in a half-space and a complementary solution that enforces the boundary conditions. The latter is non-singular and obtained from a finite element solution. The lattice resistance to dislocation motion, dislocation nucleation, dislocation interaction with obstacles and dislocation annihilation are incorporated into the formulation through a set of constitutive rules. A relation between the opening traction and the displacement jump across a cohesive surface ahead of the initial crack tip is also specified, so that crack growth emerges naturally from the boundary value problem solution. Material parameters representative of aluminum are employed. For a low density of dislocation sources, crack growth takes place in a brittle manner; for a low density of obstacles, the crack blunts continuously and does not grow. In the intermediate regime, the average near-tip stress fields are in qualitative accord with those predicted by classical continuum crystal plasticity, but with the local stress concentrations from discrete dislocations leading to opening stresses of the magnitude of the cohesive strength. The crack growth history is strongly affected by the dislocation activity in the vicinity of the growing crack tip.

Keywords: Crack tip plasticity; Dislocations; Fracture mechanisms; Crystal plasticity

* Corresponding author. Tel.: +1-401-863-2863; fax: +1-401-863-1157.
E-mail address: needle@engin.brown.edu (A. Needleman).

0022-5096/00/$ - see front matter
PII: S0022-5096(99)00076-9

1. Introduction

The interaction between plastic flow and the actual process of material separation plays an important role in setting the fracture response of structural materials. For example, plastic dissipation in the material around a crack tip results in a macroscopic work of fracture that is much larger than the work required to separate the crack surfaces (e.g. Irwin, 1958; Freund, 1998; Tvergaard and Hutchinson, 1992). By way of contrast, micro- or nanoscale patterning of plastic flow can lead to dislocation-free regions and/or dislocation pile-ups that give rise to stress concentrations that promote fracture (Lin and Thomson, 1986; Shastry et al., 1994).

Analyses using classical continuum plasticity have provided much insight into the interaction between plastic flow and fracture processes. However, when the actual separation process takes place on an atomic scale there is an inherent difficulty in using continuum plasticity. According to classical continuum plasticity, the maximum stress attained at a blunted mode I crack tip is of the order of three to five times the material's flow strength. Typically, such stress levels are too low to cause atomic separation. This is of particular significance when cohesive surface models of fracture are used in conjunction with continuum plasticity, as in Needleman (1990) and Tvergaard and Hutchinson (1992).

Experimental evidence (Fleck et al., 1994; Ma and Clarke, 1995; De Guzman et al., 1993), suggests that plastic flow over small material size scales requires higher stress levels than does plastic flow over larger size scales. Nonlocal plasticity theories have been developed, e.g. Fleck and Hutchinson (1993, 1997), Acharya and Bassani (2000), to model this effect. Such theories can give rise to higher stress levels in the vicinity of a crack tip than do classical plasticity theories (e.g. Wei and Hutchinson, 1997). A nonlocal plasticity theory implicitly attributes the increased stress to concentrations associated with dislocation structures. Another model, proposed by Suo et al. (1993), and used, for example, by Beltz et al. (1996), postulates a dislocation-free zone as an elastic strip inside which the crack propagates. Because the strip remains elastic, stresses become high enough for atomic separation to develop. Both of these approaches aim at a continuum description of plastic flow and crack propagation, so that the effect of the discreteness of the actual dislocation structure is still not taken into account.

In this paper, we carry out full boundary value problem solutions for small scale yielding of a mode I crack in plane strain, with plastic flow arising from the collective motion of large numbers of edge dislocations. The fracture properties of the material are embedded in a cohesive surface constitutive relation so that crack initiation and crack growth emerge as natural outcomes of the boundary value problem solution. The formulation and solution of the boundary value problem for the dislocated solid follows the approach of Van der Giessen and Needleman (1995) and Cleveringa et al. (1999a). The stresses and strains are written as superpositions of fields due to the discrete dislocations, which are singular inside the body, and image fields that enforce the boundary conditions. With attention restricted to small strains, the nonlinear boundary value problem for the smooth

image fields can be conveniently solved by an incremental finite element method. In this approach, the long range interactions between dislocations are accounted for through the continuum elasticity fields. Drag during dislocation motion, interactions with obstacles, and dislocation nucleation and annihilation are also accounted for. These are not represented by the elasticity description of dislocations and are incorporated into the formulation through a set of constitutive rules, which are based on those proposed by Kubin et al. (1992).

A key aspect of the formulation here is that both the plastic stress–strain response and the evolution of the dislocation structure are outcomes of the solution of the boundary value problem. By way of contrast, in a conventional continuum formulation the plastic stress–strain response is an input (Rice, 1987; Cuitiño and Ortiz, 1992), while early dislocation analyses have postulated a dislocation structure in the crack tip vicinity (e.g. Weertman et al., 1983). More recently, dislocation dynamics studies have been carried out where the dislocation structure evolved in response to the imposed loading; near a stationary mode I crack tip by e.g. Hirsch and Roberts (1989), Nitzsche and Hsia (1994), and near a mode III growing crack by Zacharopoulos et al. (1997). A main focus in these studies has been the ductile-brittle transition in initially dislocation-free materials, where dislocations are nucleated from the crack tip. However, in many materials the pre-existing dislocations have an important influence on the fracture toughness (e.g. Ashby and Embury, 1985). In the spirit of an analysis by Lin and Thomson (1986), Shastry et al. (1994) used an essentially one-dimensional model for mode II conditions to study the influence of pile-ups of existing dislocations near the crack tip on the ductile-brittle transition.

The focus in this paper is on materials that need not be dislocation-free initially. Initially present dislocations may serve either as bulk sources for dislocation generation or as obstacles to dislocation motion. The computations are carried out in the framework of small-scale yielding. This is imposed by prescribing displacements corresponding to the isotropic, linear elastic mode I singular fields remote from the crack tip with a monotonically increasing stress intensity factor. The potentially activated slip planes have no mobile dislocations initially, and nucleation of dislocations takes place from a density of two-dimensional Frank–Read sources randomly distributed in a process window surrounding the crack tip. A density of obstacles is also distributed within this process window. The evolution of plasticity and the history of crack growth emerge from the boundary value problem solutions. The results to be presented particularly focus on the effects of source and obstacle densities on the material's crack growth resistance.

2. Problem formulation

Small- scale yielding conditions are considered so that plastic flow is assumed to be confined to a small region near the current crack tip. As illustrated in Fig. 1, this region is represented by a window in which plastic flow is caused by the motion of discrete dislocations. There are no dislocations outside this window.

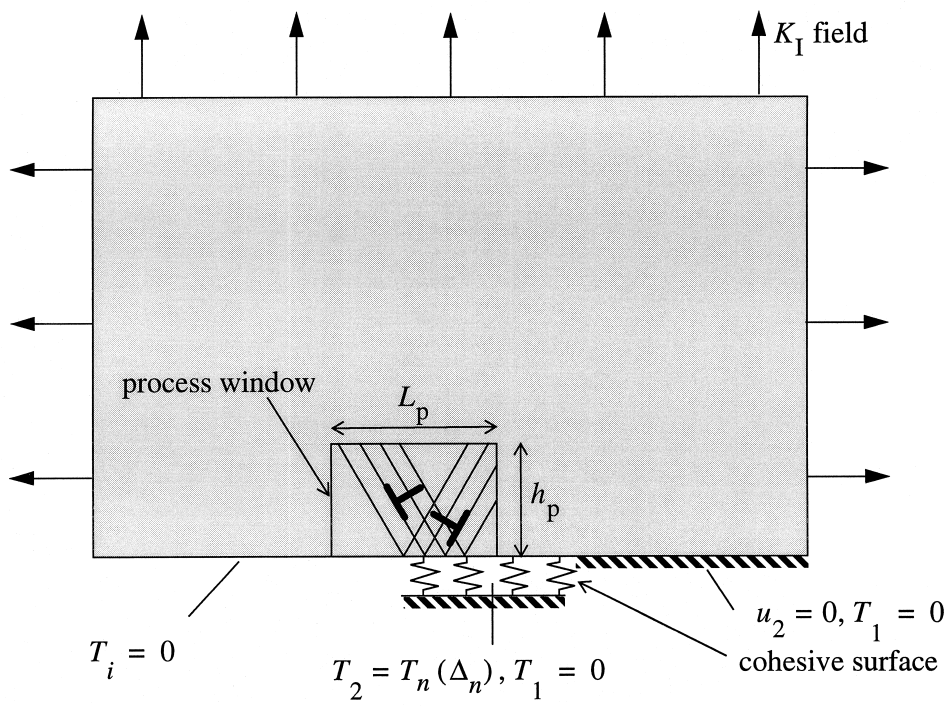

Fig. 1. Small-scale yielding analysis under mode I conditions with discrete dislocations moving inside a process window. Because of symmetry, only half the problem needs to be analyzed. The cohesive surface ahead of the initial crack is used to describe crack growth.

The dislocations are treated as line singularities in elastically isotropic material, with Young's modulus E and Poisson's ratio ν. Multiple slip is accounted for, with slip planes being oriented symmetrically about the crack plane. Crack growth is modeled using a cohesive surface framework where the fracture characteristics of the material are embedded in a traction–displacement separation relation (Needleman, 1987). There is a single cohesive surface that extends over a distance of x_c in front of the initial crack. When symmetry about the crack line is assumed, the analysis can be limited to the region shown in Fig. 1.

Cartesian tensor notation is adopted and for small strains, with body forces neglected, the principle of virtual work then takes the form

$$\int_V \sigma_{ij}\delta\epsilon_{ij}\,\mathrm{d}V - \frac{1}{2}\int_{S_{\mathrm{coh}}} T_i\delta\Delta_i\,\mathrm{d}S = \int_{S_{\mathrm{ext}}} T_i\delta u_i\,\mathrm{d}S. \tag{1}$$

Here, V is the volume of the region analyzed, S_{ext} is the external surface and S_{coh} is the surface across which cohesive tractions operate. Further, σ_{ij} are the components of the stress tensor, u_i are the displacement field components, Δ_i are the components of the displacement jump across the cohesive surface and

$$\epsilon_{ij} = \frac{1}{2}(u_{i,j} + u_{j,i}), \tag{2}$$

$$T_i = \sigma_{ij} \nu_j, \tag{3}$$

with ν_i the components of the unit outward normal on S_{coh} or S_{ext}. The factor 1/2 in Eq. (1) stems from the fact that, by virtue of symmetry, only half of the work in the cohesive surface contributes to the work in the region analyzed.

The small scale yielding boundary conditions involve imposing displacements corresponding to the elastic mode I singular field remote from the crack tip. For an isotropic elastic solid, with the initial crack tip at the origin, the displacements on the remote boundary of the region analyzed are

$$u_1 = \frac{K_{\text{I}}}{\mu}\sqrt{\frac{r}{2\pi}}\cos\frac{\theta}{2}\left(1 - 2\nu + \sin^2\frac{\theta}{2}\right) \tag{4}$$

$$u_2 = \frac{K_{\text{I}}}{\mu}\sqrt{\frac{r}{2\pi}}\sin\frac{\theta}{2}\left(2 - 2\nu - \cos^2\frac{\theta}{2}\right) \tag{5}$$

where

$$r = \sqrt{x_1^2 + x_2^2} \quad \theta = \tan^{-1}\left(\frac{x_2}{x_1}\right), \tag{6}$$

$\mu = E/2(1+\nu)$ and K_{I} is the mode I stress intensity factor.

Since the initial crack is at the origin,

$$T_1(x_1, 0) = T_2(x_1, 0) = 0 \quad \text{for } x_1 < 0. \tag{7}$$

The cohesive constitutive relation for the normal traction is taken to have the form of the exponential universal binding law of Rose et al. (1981) for which

$$T_{\text{n}}(\Delta_{\text{n}}) = -\sigma_{\max}\frac{\Delta_{\text{n}}}{\delta_{\text{n}}}\exp\left(-\frac{\Delta_{\text{n}}}{\delta_{\text{n}}} + 1\right) \quad \text{for } 0 < x_1 < x_{\text{c}} \tag{8}$$

with Δ_{n} being the normal separation of the cohesive surface and T_{n} the corresponding traction. The normal to the cohesive surface is parallel to the x_2-axis so that, with the assumed symmetry, the opening of the cohesive surface, Δ_{n}, is given by

$$\Delta_{\text{n}} = 2u_2(x_1, 0). \tag{9}$$

Because of the assumed symmetry, the tangential traction vanishes on the cohesive surface, $T_1(x_1, 0) = 0$ for $0 < x_1 < x_c$.

Ahead of the cohesive surface, symmetry conditions are prescribed so that

$$T_1(x_1, 0) = 0, \quad u_2(x_1, 0) = 0 \qquad \text{for } x_1 > x_c. \tag{10}$$

3. Method of analysis

The computation of the deformation history is carried out in an incremental manner with a monotonically increasing value of K_I prescribed in Eqs. (4) and (5). Each time step involves three main computational stages: (i) determining the Peach–Koehler forces on the dislocations; (ii) determining the rate of change of the dislocation structure, caused by the motion of dislocations, the generation of new dislocations, their mutual annihilation, and their possible pinning at obstacles; and (iii) determining the stress and strain state for the updated dislocation arrangement.

At a given stage of loading, the velocity, strain-rate and stress-rate fields are written as the superposition of two fields,

$$\dot{u}_i = \tilde{\dot{u}}_i + \hat{\dot{u}}_i, \quad \dot{\epsilon}_{ij} = \tilde{\dot{\epsilon}}_{ij} + \hat{\dot{\epsilon}}_{ij}, \dot{\sigma}_{ij} = \tilde{\dot{\sigma}}_{ij} + \hat{\dot{\sigma}}_{ij} \tag{11}$$

The ($\tilde{}$) fields are the fields of the individual dislocations, in their current configuration, and give rise to tractions $\tilde{T}_i$ and displacements $\tilde{U}_i$ on the boundary of the body. Here, the individual dislocation fields are those for an edge dislocation in a traction-free half-space (Freund, 1994), with the traction-free surface corresponding to the crack plane $x_2 = 0$. These dislocation fields are given in Appendix A. The ($\hat{}$) fields represent the image fields that correct for the actual boundary conditions, as follows.

At a given time t, the stress field and the current positions of all dislocations are known. An increment of loading $\dot{K}_I \Delta t$ is prescribed. The rate boundary value problem is formulated by expanding the virtual work balance (1) at $t + \Delta t$

$$\int_V \hat{\sigma}_{ij}^{(t+\Delta t)} \delta\epsilon_{ij} \, \mathrm{d}V - \frac{1}{2} \int_{S_{coh}} T_n^{(t+\Delta t)} \delta\Delta_n \, \mathrm{d}S = 0. \tag{12}$$

The expression (12) has been simplified relative to Eq. (1) by using $T_i = 0$ on those parts of the external surface S_{ext} on which tractions are prescribed, and by invoking $\delta u_i = 0$ on that part of the external surface where the displacements are prescribed and the vanishing of the tangential traction on the cohesive surface. We have also used the fact that the individual dislocation fields $\tilde{\sigma}_{ij}$ satisfy continuing equilibrium together with traction-free conditions on $x_2 = 0$, so that $\int_V \tilde{\sigma}_{ij} \delta\epsilon_{ij} \, \mathrm{d}V = 0$.

A Taylor series expansion for the cohesive traction about the state at $t + \Delta t$ gives

$$T_n\left(\Delta_n^{(t+\Delta t)}\right) = T_n\left(\tilde{\Delta}_n^{(t+\Delta t)} + \hat{\Delta}_n^{(t+\Delta t)}\right) = T_n\left(\tilde{\Delta}_n^{(t+\Delta t)} + \hat{\Delta}_n^{(t)} + \hat{\dot{\Delta}}_n t\right)$$

$$= T_n\left(\tilde{\Delta}_n^{(t+\Delta t)} + \tilde{\Delta}_n^{(t)}\right) - K_n\left(\tilde{\Delta}_n^{(t+t)} + \hat{\Delta}_n^{(t)}\right)\hat{\dot{\Delta}}_n \Delta t \tag{13}$$

where $\tilde{\Delta}_n$ and $\hat{\Delta}_n$ are related to the corresponding displacement fields $\tilde{u}_2$ and $\hat{u}_2$ through (9), a superposed dot denotes differentiation with respect to time t and where

$$K_n = -\frac{\partial T_n}{\partial \Delta_n}. \tag{14}$$

Also, to first order,

$$\hat{\sigma}_{ij}^{(t+\Delta t)} = \hat{\sigma}_{ij}^{(t)} + \dot{\hat{\sigma}}_{ij}\Delta t \tag{15}$$

Substituting Eqs. (13) and (15) into the principle of virtual work (12) gives

$$\begin{aligned}&\int_V \dot{\hat{\sigma}}_{ij}\delta\epsilon_{ij}\,\mathrm{d}V + \frac{1}{2}\int_{S_{coh}} K_n\left(\tilde{\Delta}_n^{(t+\Delta t)} + \hat{\Delta}_n^{(t)}\right)\dot{\hat{\Delta}}_n\delta\Delta_n\,\mathrm{d}S \\ &\quad = -\frac{1}{\Delta t}\left[\int_V \hat{\sigma}_{ij}^{(t)}\delta\epsilon_{ij}\,\mathrm{d}V - \frac{1}{2}\int_{S_{coh}} T_n\left(\tilde{\Delta}_n^{(t+\Delta t)} + \hat{\Delta}_n^{(t)}\right)\delta\Delta_n\,\mathrm{d}S\right]\end{aligned} \tag{16}$$

Since the (ˆ) fields are smooth in the region of interest, the rate boundary value problem in Eq. (16) is conveniently solved using a finite element method. The kinematic boundary conditions (4), (5) and (10) infer boundary conditions for the displacement rates $\dot{\hat{u}}_i$ along the same boundaries,

$$\dot{\hat{u}} = \dot{u}_i - \dot{\tilde{u}}_i \tag{17}$$

with the $\dot{\tilde{u}}_i$ fields derived from the displacement fields of the moving dislocations (see Appendix A).

Assuming dislocation glide only, the variation of the potential energy of the body due to infinitesimal variations of the position of the Ith dislocation is governed by the Peach–Koehler force $f^{(I)}$ given by

$$f^{(I)} = n_i^{(I)}\left(\hat{\sigma}_{ij} + \sum_{J\neq I}\sigma_{ij}^{(J)}\right)b_j^{(I)}, \tag{18}$$

with $n_i^{(I)}$ the slip plane normal and the Burgers vector $b_i^{(I)}$ of dislocation I. The direction of this force is in the slip plane and normal to the dislocation line. The Peach–Koehler force includes the long-range interactions with all other dislocations in the material. It is this force that will determine the evolution of the dislocation structure, accounting for glide, generation, annihilation and pinning at obstacles according to a set of rules that will be discussed subsequently.

The magnitude of the glide velocity $v^{(I)}$ of dislocation I is taken to be linearly related to the Peach–Koehler force through the drag relation

$$f^{(I)} = Bv^{(I)} \tag{19}$$

where B is the drag coefficient. As in Cleveringa et al. (1999a), a cut-off velocity of

20 m/s is used which is low enough to be effective in allowing substantially increased time steps and high enough not to effect the results significantly.

New dislocation pairs are generated by simulating Frank–Read sources. The initial dislocation segment of a Frank–Read source bows out until it produces a new dislocation loop and a replica of itself. The Frank-Read source is modeled in terms of a critical value of the Peach–Koehler force, the time it takes to generate a dislocation loop and the size of the generated loop. In two dimensions, this is simulated by point sources which generate a dislocation dipole when the magnitude of the Peach–Koehler force at the source exceeds a critical value $\tau_{\text{nuc}}b$ during a period of time t_{nuc}. The distance L_{nuc} between the dislocations is taken to be specified by

$$L_{\text{nuc}} = \frac{E}{4\pi(1-\nu^2)}\frac{b}{\tau_{\text{nuc}}}. \tag{20}$$

At this distance, the shear stress of one dislocation acting on the other is balanced by the slip plane shear stress τ_{nuc}.

Annihilation of two dislocations with opposite Burgers vector occurs when they are sufficiently close together. This is modeled by eliminating two dislocations when they are within a material-dependent, critical annihilation distance L_{e}.

Obstacles to dislocation motion are modeled as fixed points on a slip plane. Such obstacles account for the effects of small precipitates or for dislocations on other slip systems in blocking slip. Pinned dislocations can only pass the obstacles when their Peach–Koehler force exceeds an obstacle dependent value $\tau_{\text{obs}}b$.

It is noted that the above rules for dislocation evolution are intended to incorporate short-range effects at an atomic scale which a discrete dislocation model cannot resolve. Short-range interactions between dislocations on different slip planes near their junction are not accounted for separately in this analysis; such dislocations only interact through their long-range elastic fields.

When a dislocation glides towards the open crack it can disappear from the material. We model this by taking the dislocation out of the system, but the number of dislocations that left from each slip plane is stored. Since the analytical formulas in Appendix A describe the dislocation in a half-space with a traction-free surface, a dislocation located at the surface has no contribution to the stress field, but there is a contribution to the displacement field, with a step of $b/2$ across the slip plane at the surface.

Because of the assumed symmetry, there is a mirror dislocation for each dislocation in the region analyzed numerically. This mirror dislocation does not need to be accounted for explicitly when superimposing the fields of all dislocations, for example as in the sum in Eq. (18). Rather, its presence is accounted for through the symmetry boundary conditions. What does need to be accounted for in the dislocation analysis is that when a dislocation crosses the closed crack plane, it leaves the region analyzed, but, due to symmetry, a mirror dislocation enters into the system along the mirror slip plane.

4. Results

The size of the region analyzed for the cases to be presented is 1000×500 μm and a finite element mesh of 120×100 bilinear quadrilateral elements is used. The mesh is highly refined (80×80 elements) inside the process window which is taken to have dimensions $L_p = 10$ μm by $h_p = 12.5$ μm (see Fig. 1). In all cases, the crystal has two slip systems, symmetrically oriented at $+60^\circ$ and -60° to the crack plane $x_2 = 0$. For each slip system there are 401 slip planes equally spaced over the process window, with a spacing of $86b$. Initially, these slip planes are assumed not to have any mobile dislocations, but to have a random distribution of dislocation sources and obstacles. One of the source and obstacle distributions used is shown in Fig. 2; there is no special dislocation nucleation from the crack tip.

The value of the drag coefficient in Eq. (19) is taken as $B = 10^{-4}$ Pa s, which is a representative value for aluminum (Kubin et al., 1992). The strength of the dislocation sources is randomly chosen from a Gaussian distribution with mean strength $\bar{\tau}_{nuc} = 50$ MPa and standard deviation $0.2\bar{\tau}_{nuc}$. From Eq. (20) the mean nucleation distance is $L_{nuc} = 125b$ and b is specified to have the value 0.25 nm.

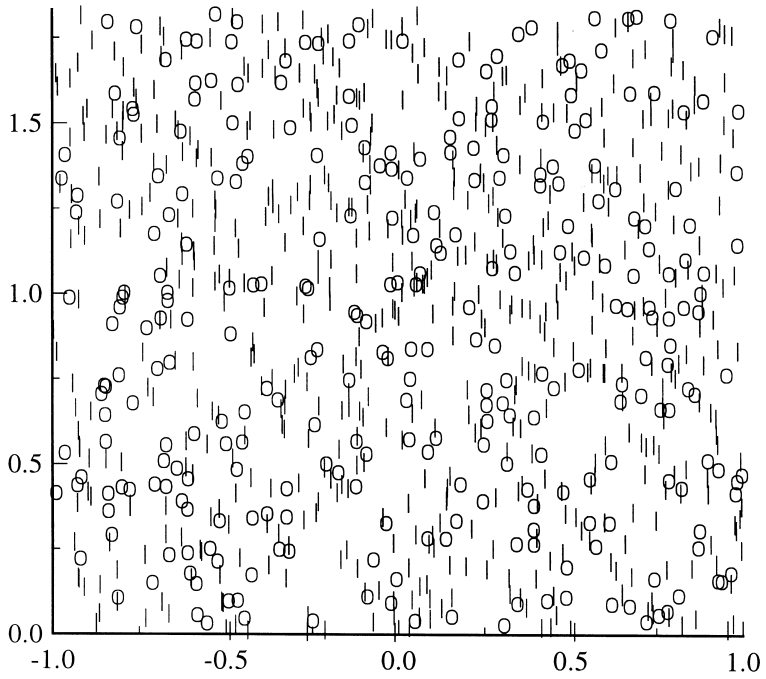

Fig. 2. Dislocation source and obstacle distribution within a 2×2 μm region around the initial crack tip for the case with $\rho_{nuc} = 49$ μm^{-2} and $\rho_{obs} = 98$ μm^{-2}. The dislocation sources are represented by "o" and the obstacles by "|".

The nucleation time for all sources is taken as $t_{nuc} = 0.01$ μs. All obstacles are taken to have the same strength $\tau_{obs} = 150$ MPa. The annihilation distance is specified as $L_e = 6b$ (Kubin et al., 1992). The elastic constants are taken as $E = 70$ GPa and $\nu = 0.33$ giving a shear modulus μ of 26.3 GPa.

The cohesive surface properties are taken to be $\sigma_{max} = 0.6$ GPa and $\delta_n = 4b$ giving a work of separation, $\phi_n = \exp(1)\sigma_{max}\delta_n$ of 1.63 J/m^2. For fracture without any dislocation activity, so that all energy released is consumed by the cohesive surface, unstable crack growth occurs at an applied stress intensity factor K_0 of (Rice, 1968),

$$K_0 = \sqrt{\frac{E\phi_n}{1-\nu^2}}. \tag{21}$$

For the material parameters here $K_0 = 0.358$ MPa m$^{1/2}$.[1] All calculations have been carried out for an applied loading rate specified by $\dot{K}_I = 50$ GPa m$^{1/2}$/s.

4.1. Two limiting cases

The crack growth behavior depends on the density of sources and obstacles, and there are two limiting cases. One of these occurs when there are so few sources (of strength τ_{nuc}, low compared to σ_{max}) that very few dislocations are generated before the crack starts to propagate. In this source-limited situation, the stresses near the tip are close to those associated with the mode I elastic crack tip field, with isolated deviations caused by the few dislocations that have nucleated. One such case is illustrated in Fig. 3(a). Because of the cohesive surface, the stresses are not singular at the crack tip. The opening stress at the crack tip needs to reach the strength σ_{max} of the cohesive surface for the crack to propagate in a brittle manner.

When dislocations are generated before crack propagation, they tend to move away from the crack tip and to shield the tip. The second limiting case arises when there are insufficient obstacles (of high enough strength τ_{obs}) to pin the dislocations. In such obstacle-limited cases, the dislocations strongly relax the stresses near the tip, leading to continued blunting without crack propagation. This is shown in Fig. 3(b), where the applied K_I is almost twice as large as in the brittle case of Fig. 3(a), but crack growth has not occurred. In this case, the obstacle density is two times lower than that shown in Fig. 2, $\rho_{nuc} = \rho_{obs} = 49$ μm^{-2}. In Fig. 3(b), on average, the stresses within a distance of about 5 μm are rather uniform inside the two sectors $0^\circ < \theta < 60^\circ$ and $60^\circ < \theta < 120^\circ$. Although each dislocation has a singular stress field that decays inversely proportional with distance, for plotting purposes the stresses are extrapolated to the nodes of the

[1] In the preliminary study of Cleveringa et al. (1999b), the value of K_0 reported should be corrected by dividing it by a factor of $\sqrt{2}$.

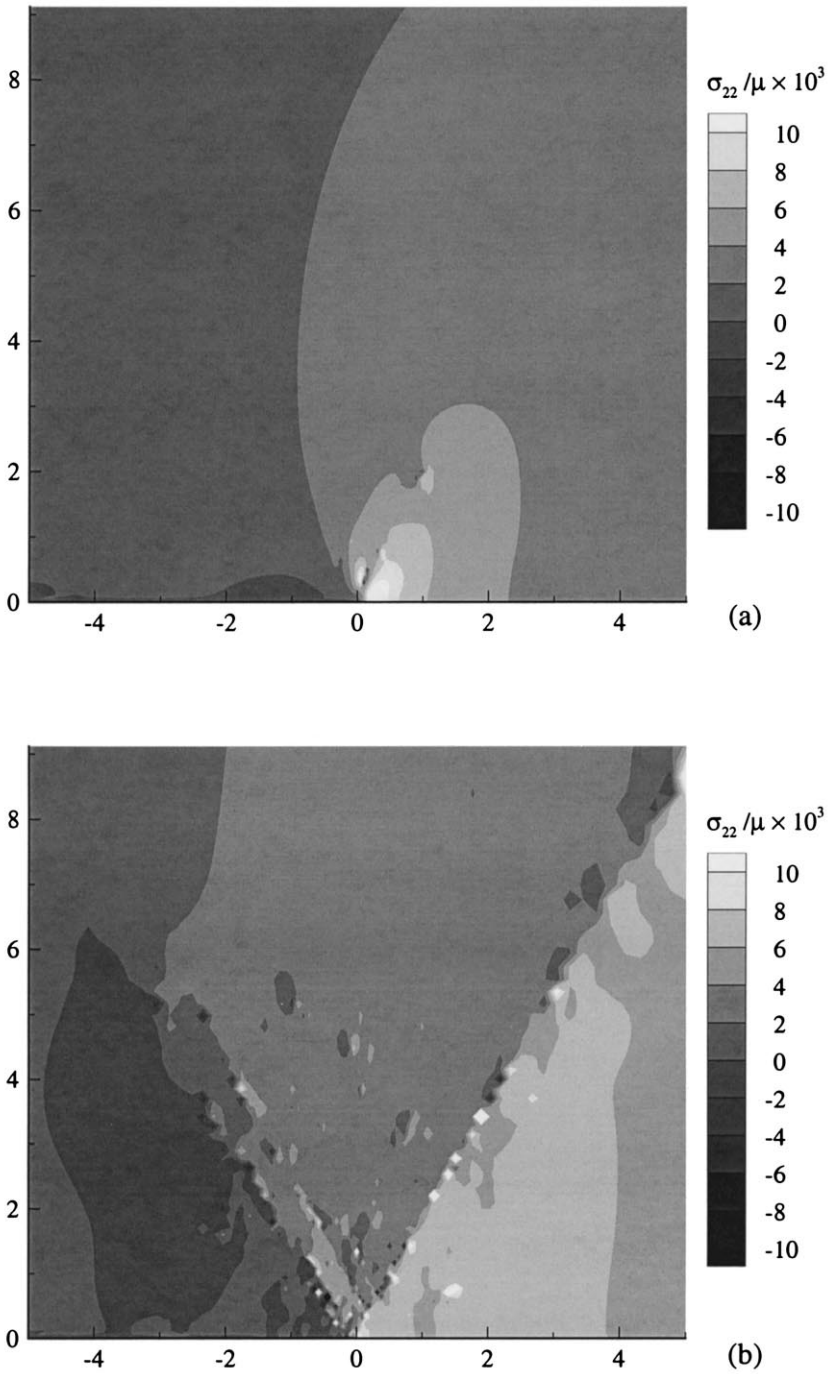

Fig. 3. Distributions of the opening stress σ_{22} for two limiting situations: (a) source limited plasticity leading to completely brittle fracture at $K/K_0 = 1$; (b) obstacle limited plasticity leading to strong blunting with no tendency for crack propagation prior to $K/K_0 = 1.86$.

finite element mesh. As a consequence, the local high stresses around each dislocation are not seen in the contour plot.

Rice (1987) obtained asymptotic solutions for the stress distributions in plane strain mode I crack tip fields for elastic-ideally plastic FCC and BCC crystals. Similar stress distributions were seen in the numerical results of Cuitiño and Ortiz (1992). The near-tip stress state involves angular sectors within which the stress state is constant, with the stress discontinuous across sector boundaries. The analysis by Rice (1987) can be readily repeated for a double slip system with the slip planes at 60° and 120° as in the present dislocation analysis, leading to three sectors: (0, 60°), (60°, 120°) and (120°, 180°). The stresses inside these sectors can be computed from the yield condition on the slip systems (with slip system flow strength τ_0), the boundary conditions and the traction continuity conditions across the sector boundaries (see Rice, 1987). The resulting opening stresses in the three sectors are $4\sqrt{3}\tau_0$, $2\sqrt{3}\tau_0$ and 0, respectively. The mean normal stress $(\sigma_{11}+\sigma_{22})/2$ in the sector ahead of the crack tip is $10/\sqrt{3}\tau_0$. In Fig. 3(b), the average value of σ_{22} in the sector ahead of the crack is ≈ 150 and ≈ 75 MPa in the sector above the crack. The factor of 2 difference coincides with the ratio from the above continuum slip analysis. Other average stress components (not shown) also agree well.

4.2. Effect of source and obstacle density

The curves of applied K_{I} versus crack advance Δa in Figs. 4 and 5 show how the fracture behavior depends on the density of sources and obstacles. The crack location in these figures is taken to be the point along the cohesive surface where the opening of the cohesive surface, Δ_{n}, is $2\delta_{\mathrm{n}}$.

Fig. 4 shows results for three densities of randomly placed sources and, for comparison purposes, the result for a dislocation-free material. The general trend is that the value of the applied K_I for crack growth initiation as well as the crack growth resistance increases with an increasing density of dislocation sources. Part of the small deviation of the initiation value of K_{I} from K_0 in Fig. 4 for $\rho_{\mathrm{nuc}}=0$ stems from using $2\delta_{\mathrm{n}}$ to define the crack location and part is a consequence of discretization error. More dislocations are generated with an increasing density of sources so that, before crack advance, the increasing number of dislocations leads to stronger blunting of the crack tip, thus raising the value of the applied K_{I} necessary for initiation. As the crack propagates, the increasing dislocation activity tends to shield the tip, leading to an increasing resistance to further crack growth.

It is also seen that crack growth tends to proceed in "spurts," especially for the lower source densities. For a density of 4.1 $\mu\mathrm{m}^{-2}$, the initiation of crack growth takes place at the same value as for the source-free material, and the crack rapidly grows with a resistance that is slightly higher than K_0, indicating that a few dislocations are generated during crack growth. At $\Delta a \approx 0.5$ μm, the resistance increases significantly followed by another rapid extension of about 0.15 μm, etc. When the density of sources is increased, the periods of brittle crack advance

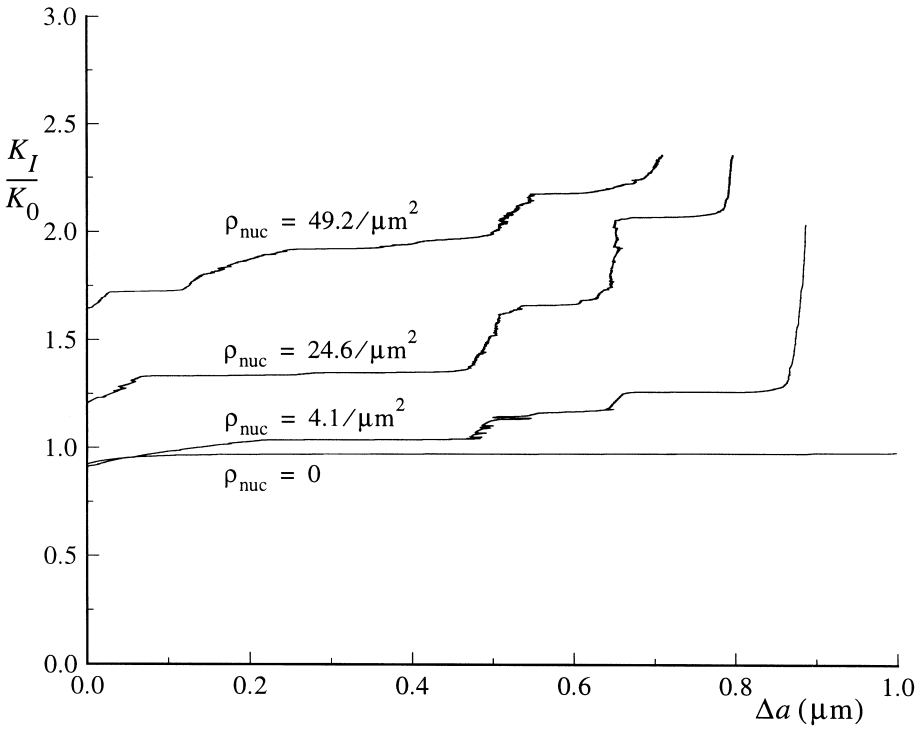

Fig. 4. Normalized applied stress intensity factor K_I/K_0 vs. crack extension Δa for various densities of dislocation sources. The obstacle density is $\rho_{obs} = 98\ \mu m^{-2}$.

shorten ($\rho_{nuc} = 24.6\ \mu m^{-2}$) and gradually disappear ($\rho_{nuc} = 49.2\ \mu m^{-2}$). The strong increase of the crack growth resistance for $\rho_{nuc} = 4.1\ \mu m^{-2}$ at around $\Delta a = 0.9\ \mu m$ is due to the fact that the crack tip has, by coincidence, approached a dislocation source which then generates many dislocations. A similar phenomenon occurs for $\rho_{nuc} = 24.6\ \mu m^{-2}$ after 0.8 μm of crack growth.

Close examination of the results reveals that many sources, distributed over a significant part of the dislocated region have actually generated dislocations. The first few dislocations are generated from sources with relatively low strength that are located close to the tip. When these dislocations move away from the crack they can subsequently activate sources in the interior of the material. This autocatalytic process is operating especially in the cases with the higher source densities.

Fig. 5 summarizes the results for simulations with four obstacle densities at a source density of 49 μm^{-2} (the curve for $\rho_{obs} = 98\ \mu m^{-2}$, $\rho_{nuc} = 49\ \mu m^{-2}$ is common to both figures). The general trend in this figure is that the crack growth resistance increases with a decreasing density of obstacles. However, the results do not completely order by obstacle density, so that this tendency is modified significantly by statistical effects. For the lowest density shown, $\rho_{obs} = 49\ \mu m^{-2}$,

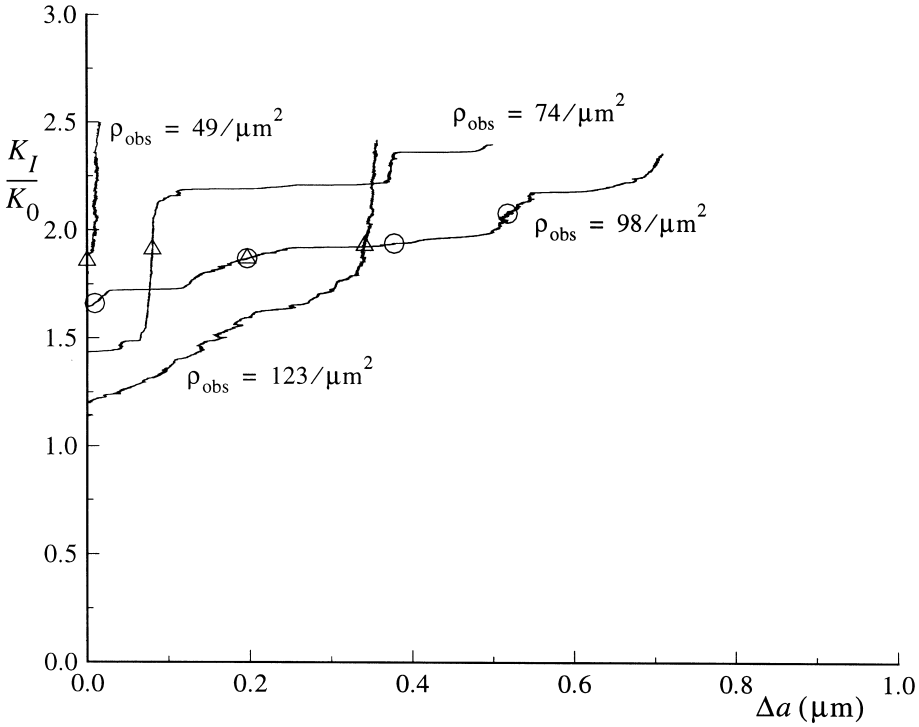

Fig. 5. Normalized applied stress intensity factor K_I/K_0 vs. crack extension Δa for various densities of obstacles. The source density is $\rho_{nuc} = 49\ \mu m^{-2}$. Dislocation distributions corresponding to the triangles are shown in Fig. 6, while the circles correspond to Fig. 7.

the crack does not initiate until $K_I \approx 1.9K_0$ and after little growth the resistance rises rapidly. In this case, the dislocations that have been generated give rise to strong blunting of the crack and to effective crack-tip shielding. An increasing density of obstacles tends to prevent dislocations moving away from the crack tip, thus promoting earlier initiation of crack propagation. Indeed, the total dislocation densities at crack initiation (5.7, 3.1, 5.7 and 2.1 μm^{-2} for increasing obstacle density) order with the initiation values in Fig. 5. It should be noted, however, that the crack initiation behavior is controlled mainly by the relatively small number of dislocations very near the crack tip.

An impression of the dislocation structures that develop for different obstacle densities can be obtained from Fig. 6. It should be noted that the dislocation distributions are shown here at the same value of K_I, so that, as shown by the triangles in Fig. 5, the different cases exhibit different amounts of crack advance. The amount of crack growth can also be seen in the crack profiles shown in Fig. 6. For the lower two densities, Fig. 6(a) and (b), the dislocation activity is mostly concentrated on a few (say, five) of the slip planes emanating from near the initial crack tip. Especially in Fig. 6(a), there are many dislocations on the -60° slip

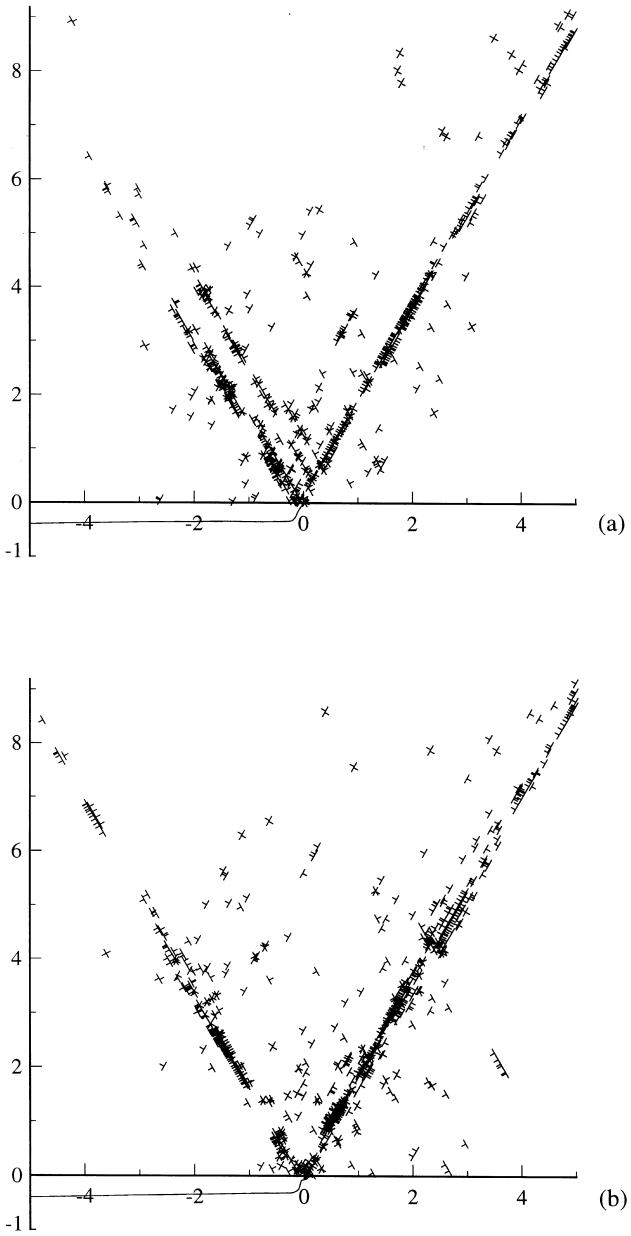

Fig. 6. Dislocation distributions inside the 10 × 12.5 μm process window at an applied loading of $K_I/K_0 \approx 1.87$ for the four different obstacle densities shown in Fig. 6 (see triangles): $\rho_{obs} = 49\ \mu m^{-2}$ (a); $74\ \mu m^{-2}$ (b); $98\ \mu m^{-2}$ (c); $123\ \mu m^{-2}$ (d). The corresponding crack opening profiles (displacements magnified by a factor of 10) are plotted below the x_1-axis.

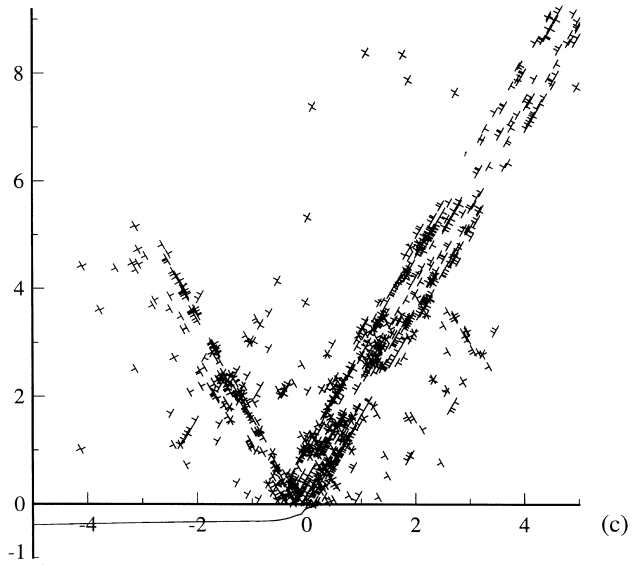

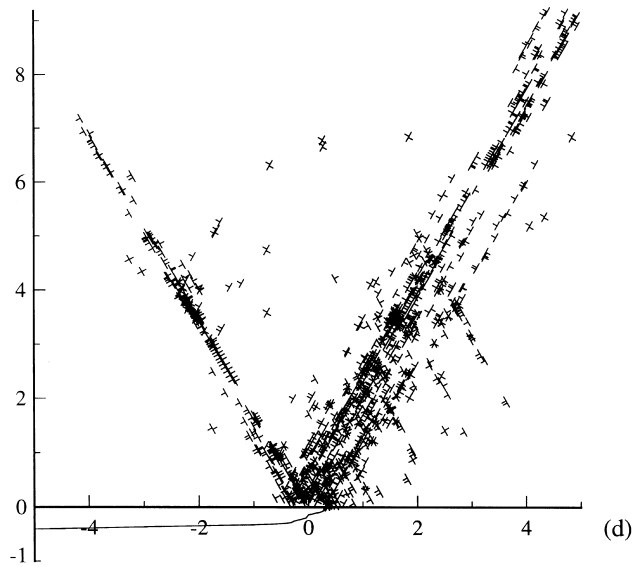

Fig. 6 (*continued*)

planes, but with increasing obstacle density most of the dislocations are located on the 60° planes. The shielding dislocations on these slip planes (with the Burgers vector pointing away from the crack plane) arrange in pile-ups formed from the obstacles on these planes. However, we also see that the dynamic process of dislocation generation and motion has led to quite a significant density of anti-shielding dislocations on adjacent slip planes. With increasing obstacle density, some crack advance has taken place at the value of K_I considered here, Fig. 6(c) and (d), and crack growth has given rise to dislocation activity on 60° slip planes that were ahead of the initial crack tip. Crack growth does not appear to substantially increase the dislocation activity on the −60° planes. However, in Fig. 6(c) and (d), a noticeable number of dislocations have appeared in the wedge $\theta < 60°$. It is worth noting that the dislocation structures shown in these and forthcoming figures are not equilibrium distributions but instantaneous snapshots. Due to the continuously increasing applied load and also because of the absence of a friction stress, there is no time for the dislocations to reach equilibrium positions in the present simulations.

The dislocation density in the immediate neighborhood of the moving crack tip is so high that it is difficult to ascertain the near-tip dislocation structure. Therefore, Fig. 7 shows a smaller 2×2 μm region around the initial crack tip for the case with $\rho_{nuc} = 49\ \mu m^{-2}$ and $\rho_{obs} = 98\ \mu m^{-2}$. Four different stages are shown, as indicated by the circles in Fig. 5. The first stage clearly shows that dislocation activity on slip planes emanating from behind the initial crack tip are responsible for the blunting. At this scale, the stress fields of the individual dislocations are quite noticeable, although it is recalled that the finite element mesh onto which the dislocation stresses have been extrapolated for plotting purposes is not fine enough to show the singularity of each dislocation. Despite shielding of the crack tip by dislocations, the opening stress, σ_{22}, in Fig. 7(a) reaches sufficiently high values over a distance of about 0.2 μm ahead of the tip to open the cohesive surface. To indicate the stress enhancement involved, the discrepancy between the "continuum" stress level, i.e. the average value in the sector ahead of the crack, and the cohesive strength is a factor of 3–4. The stress peak in Fig. 7(a) is directly due to the presence of the discrete dislocations since quite a few dislocations are located very near the original crack tip.

With continued loading, these stresses cause the crack to propagate into the region of relatively lower stresses. Here, the crack arrests and dislocations on more forward slip planes blunt the tip again. Still, the tractions along the cohesive surface are large enough to cause opening, Fig. 7(b). One of the noticeable differences with the state shown in Fig. 7(a) is that there is a small region of about 0.1 μm around the current crack tip where there are no dislocations. Outside this region, there are a few dislocations ahead of the crack tip, which have a considerable influence on the near tip stress field. With continued loading, the crack continues to propagate in an almost brittle manner. At the stage shown in Fig. 7(c) a tangle of dislocations has formed immediately around the current tip which produces a traction profile ahead of the tip that apparently leads to rapid propagation. Fig. 7(d) shows a stage in which some blunting again accompanies

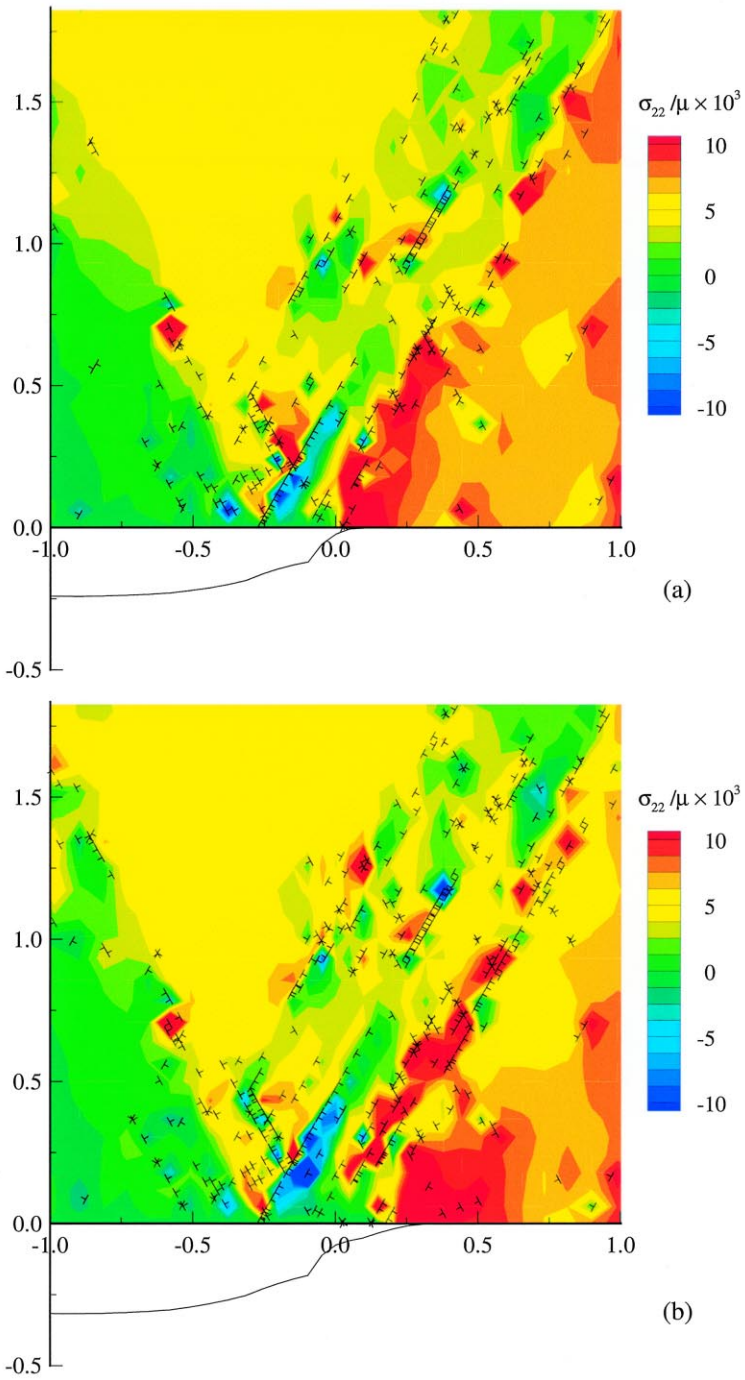

Fig. 7. Distribution of dislocations and the opening stress σ_{22} in the immediate neighborhood (2×2 μm) of the crack tip for the case with $\rho_{\text{nuc}} = 49\ \mu\text{m}^{-2}$ and $\rho_{\text{obs}} = 98\ \mu\text{m}^{-2}$ at four different stages of loading (see circles in Fig. 5): $K_{\text{I}}/K_0 = 1.66$ (a); 1.87 (b); 1.94 (c); 2.08 (d). The corresponding crack opening profiles (displacements magnified by a factor of 10) are plotted below the x_1-axis.

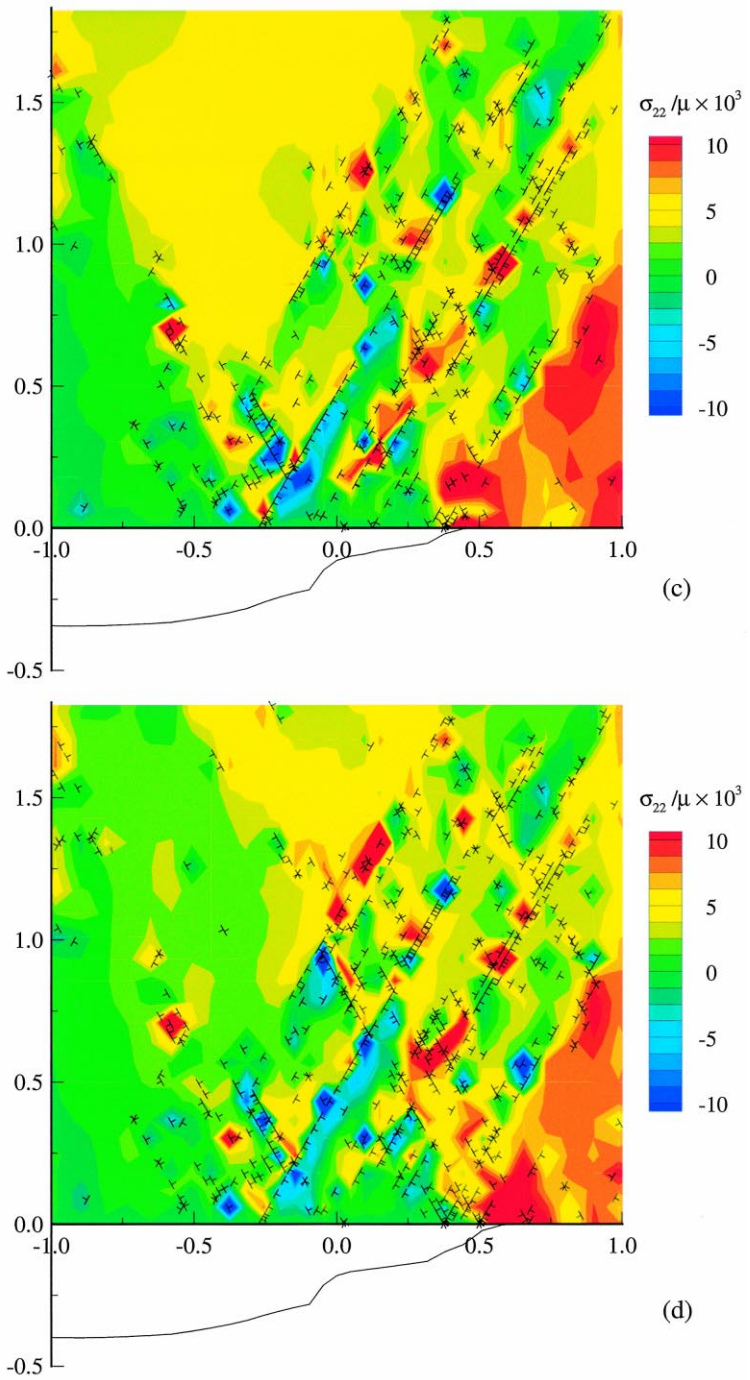

Fig. 7 (*continued*)

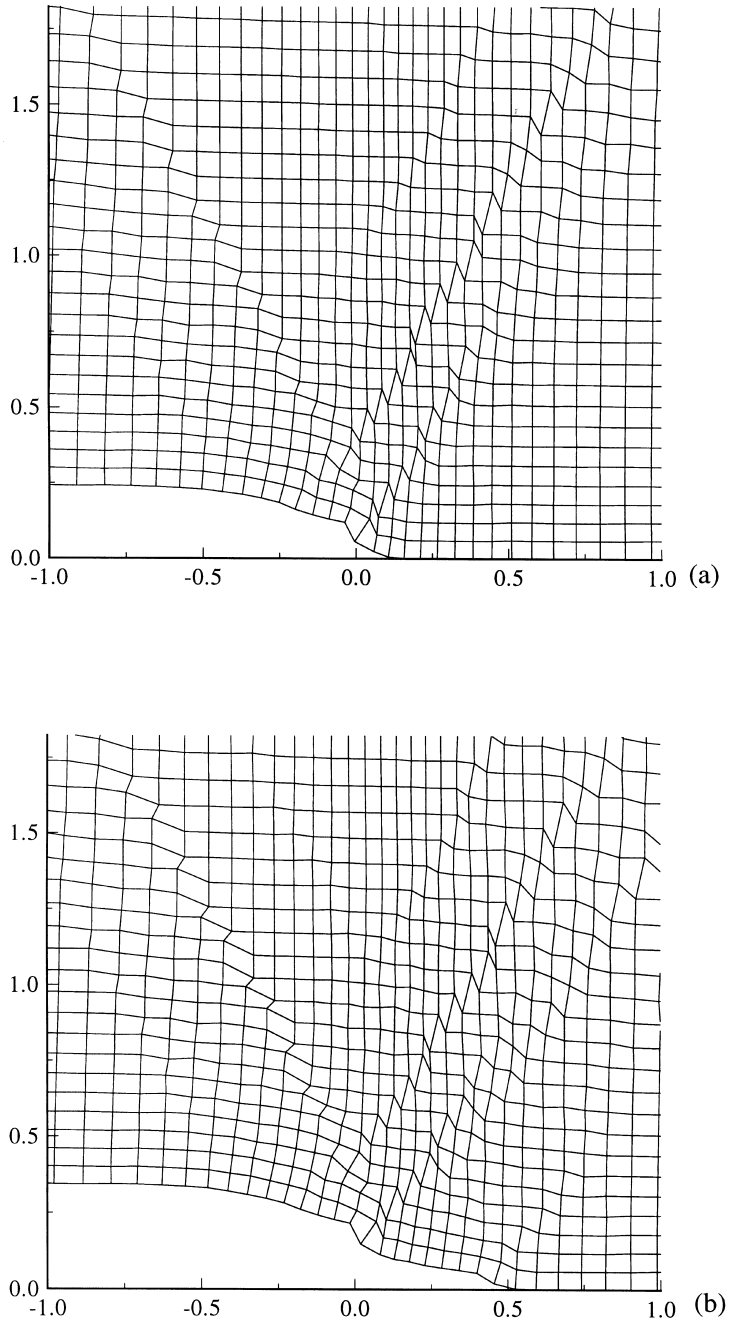

Fig. 8. Deformed meshes showing the slip pattern in the vicinity of the crack tip for the case shown in Fig. 7. The displacements are magnified by a factor of 10: (a) at $\Delta a = 0.01$ μm, $K_I/K_0 = 1.66$ corresponding to Fig. 7(a); (b) at $\Delta a = 0.38$ μm, $K_I/K_0 = 1.94$ corresponding to Fig. 7(c).

crack growth (cf. Fig. 5). As in Fig. 7(b), there is $a \approx 0.1$ μm-sized dislocation-free zone around the tip.

Fig. 8 gives an impression of the appearance of plastic deformation caused by the collective motion of the dislocations for the case shown previously in Fig. 7. Initial blunting, Fig. 8(a), has occurred mainly by slip bands emanating from the immediate neighborhood of the initial crack tip, with two slip bands at 60° and one at -60°. When the crack has propagated to the stage shown in Fig. 8(b), some blunting of the new tip has occurred but it is less intense than the initial blunting. Consistent with this, we observe only minor slip band formation from the current crack tip. Comparison of Figs. 8(a) and (b) reveals that during crack propagation slip has accumulated only on the foremost 60° slip band, whereas the other two initial slip bands were not significantly activated further.

It should be noted that the localized deformations seen in these results are due to the discreteness of the dislocations and are therefore not sensitive to the mesh size. The long-range ($\tilde{}$) fields of the dislocations, including their discontinuous displacement fields, are handled by the analytical solution for the half space outlined in Appendix A; the finite element mesh is only used to incorporate the boundary conditions. The discrete dislocation analysis of bending of a crystal (Cleveringa et al., 1999a) also gives rise to slip bands and it has been explicitly shown there that the solution is not mesh dependent.

5. Concluding remarks

We have carried out analyses of the initiation and growth of a mode I crack where the interplay between plastic dissipation and material separation is an outcome of the boundary value problem solution. The fracture properties of the material are embedded in a cohesive surface constitutive relation and plastic flow arises from the collective motion of discrete dislocations.

Two-dimensional Frank–Read sources are distributed randomly in a process window surrounding the crack tip. No mobile dislocations are present initially; mobile dislocations can only nucleate from these sources, with no special dislocation nucleation from the crack tip. Obstacles to dislocation motion are also distributed randomly within the process window.

The fracture behavior depends sensitively on the density of dislocation sources and obstacles. For a sufficiently low density of dislocation sources, only isolated dislocations are generated and crack propagation takes place in a brittle manner. On the other hand, when ample nucleation sites are available but the obstacle density is sufficiently low, the dislocations strongly relax the near-tip stresses, resulting in continued crack tip blunting without crack propagation. Between these two extremes, crack propagation with plastic dissipation takes place. The resistance to crack growth tends to increase with an increasing density of dislocation sources and to decrease with an increasing density of obstacles. These trends are consistent with the observations of Gumbsch et al. (1998) on fracture of single crystals of tungsten, who found that the fracture toughness was largely

controlled by the availability of dislocation sources while the brittle–ductile transition was controlled by the dislocation mobility. It is also interesting to note that radiation damage can lead to dislocation pinning (e.g. Carreño-Morelli et al., 1999), which our results indicate would play a role in reducing the resistance of irradiated materials to crack propagation.

Our simulations show that discrete dislocations play a dual role in the fracture process. On the one hand, dislocation activity gives rise to values of the applied K_I at initiation that are significantly higher than for an elastic solid with same cohesive properties. In addition, there is R-curve behavior — the applied K_I tends to increase with crack length. On the other hand, it is the local stress concentration associated with discrete dislocations in the vicinity of the crack tip that leads to stress levels of the magnitude of the cohesive strength, causing the crack to propagate. A necessary condition for this is the presence of obstacles to glide, which keep dislocations in the vicinity of the crack tip. The interplay between these dual roles of the discrete dislocations causes crack growth to occur in "spurts."

During the periods that crack propagation is accompanied by significant plastic deformation, the simulations show some evidence of a "dislocation-free zone." With a size of the order of 0.1 μm for the present material parameters, this zone size is similar to or larger than those considered by Shastry et al. (1994) but is an order of magnitude smaller than the dislocation free zone sizes estimated by Suo et al. (1993). Indeed, the dislocation-free zone size in our computations is so small that the stress field inside it is primarily controlled by the stress fields of the nearby dislocations. Also, it does not leave a dislocation-free strip around the propagation tip, but oscillates in size with the spurts in crack growth. During periods of brittle crack growth, the dislocation-free zone, if any, is smaller than the length scale that the present approach can resolve.

Acknowledgements

We are pleased to acknowledge stimulating discussions with R. LeSar and D.J. Srolovitz. The work of H.H.M. Cleveringa is part of the research program of the "Stichting voor Fundamenteel Onderzoek der Materie (FOM)" which is supported financially by the "Nederlandse Organisatie voor Wetenschappelijk Onderzoek (NWO)." A. Needleman and E. Van der Giessen acknowledge support from the Materials Research Science and Engineering Center on *On Micro- and Nano-Mechanics of Materials* at Brown University (NSF Grant DMR-9632524).

Appendix A. Dislocation fields in a half-space

The method of solution used in this paper makes use of the closed-from analytical fields for a single edge dislocation in the elastic half-space $x_2 > 0$. These fields can be conveniently obtained through the complex stress function approach

of Muskhelishvili (1953) as pointed out by Freund (1994). In particular, the solution invokes Muskhelishvili's observation that the solution for a half-space can be represented in terms of a single analytic function φ of $\zeta = x_1 + ix_2$ according to

$$\tilde{\sigma}_{22} - i\tilde{\sigma}_{12} = \varphi'(\zeta) - \varphi'(\bar{\zeta}) + (\zeta - \bar{\zeta})\overline{\varphi''(\zeta)}, \tag{A1}$$

$$\tilde{\sigma}_{11} + i\tilde{\sigma}_{12} = \varphi'(\zeta) + \varphi'(\bar{\zeta}) + 2\overline{\varphi'(\zeta)} - (\zeta - \bar{\zeta})\overline{\varphi''(\zeta)}. \tag{A2}$$

The overbar denotes the complex conjugate. The displacement components can be found by integration and are given through

$$2\mu(\tilde{u}_1 + i\tilde{u}_2) = (3 - 4\nu)\varphi(\zeta) + \varphi(\bar{\zeta}) - (\zeta - \bar{\zeta})\overline{\varphi'(\zeta)}. \tag{A3}$$

Freund (1994) gives the expression of φ' for a dislocation located at a distance h from the free surface. However, he used a different coordinate system and orientation of the half-space than we consider here, see Fig. 9. A transformation of variables then yields

$$\varphi'(\zeta) = -\frac{\mu}{4\pi(1-\nu)}\left[\frac{i\bar{b}}{\zeta + ih} - \frac{ib(\zeta + ih)}{(\zeta - ih)^2} - \frac{i(\bar{b} - b)}{\zeta - ih}\right], \tag{A4}$$

where the complex variable b is defined as $b = |b|m$, with $|b|$ the magnitude of the Burgers vector and $m = \cos\phi + i\sin\phi$ indicating the slip direction.

The functions φ and φ'' to be substituted into Eq. (A3) can be obtained by integration and differentiation of the expression in Eq. (A4), respectively as

$$\varphi(\zeta) = \frac{\mu}{4\pi(1-\nu)}\left[i\bar{b}\ln\left(\frac{\zeta - ih}{\zeta + ih}\right) + \frac{2bh}{\zeta - ih}\right],$$

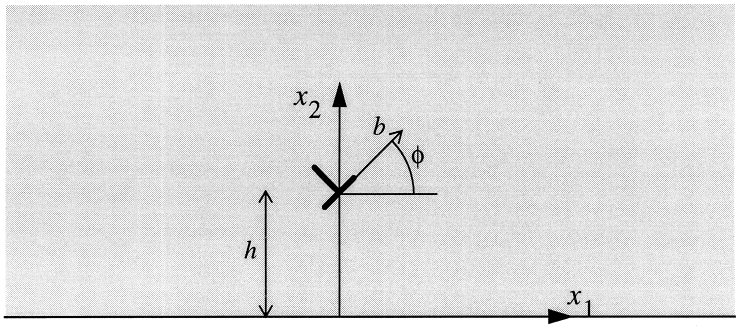

Fig. 9. Coordinate system used for the fields of a dislocation in a traction-free half-space.

$$\varphi''(\zeta) = \frac{\mu}{\pi(1-\nu)}\left[\frac{\bar{b}\zeta h}{\left(\zeta^2+h^2\right)^2} + \frac{bh}{(\zeta - ih)^3}\right]$$

It should be noted here that we have also used the opposite of the definition of b used by Freund (1994), so that the contour integral of $\tilde{u}_1 + i\tilde{u}_2$ around a dislocation in the counter clockwise direction is equal to b.

It is of importance to note that the function $\varphi(\zeta)$ is determined up to an arbitrary integration constant. This integration constant needs to be determined so that the displacement discontinuity for each dislocation properly aligns with the slip plane orientation m. The correct expression can be shown to read

$$\varphi(\zeta) = \frac{\mu}{4\pi(1-\nu)}\left[i\bar{b}\left\{\ln\left[-m(ih-\zeta)\right] - \ln\left[\bar{m}(ih+\zeta)\right]\right\} + \frac{2bh}{\zeta - ih}\right]. \tag{A5}$$

The two logarithmic terms are not to be combined in order to ensure that the branch cut aligns with the slip plane.

Finally, in order to incorporate the kinematic boundary conditions via Eq. (17) in the incremental analysis we need the expressions for the velocity components $\dot{\tilde{u}}_i$ caused by the motion of the dislocation. In deriving these, due note should be given to the fact that the real axis of the coordinate system is attached to the moving dislocation, while the imaginary (x_2) axis is fixed at the edge of the half-space. Denoting the velocity of the dislocation itself by v_i, the associated rate of change the velocity field can be obtained from the displacement field according to Eqs. (A3) and (A5) as

$$\dot{\tilde{u}}_i = \frac{\partial \tilde{u}_i}{\partial \Re(\zeta)} v_1 + \frac{\partial \tilde{u}_i}{\partial h} v_2, \tag{A6}$$

where $\Re(\zeta)$ is the real part of ζ.

References

Acharya, A., Bassani, J.L., 2000. Incompatibility and crystal plasticity. Journal of the Mechanics and Physics of Solids, in press.

Ashby, M.F., Embury, J.D., 1985. The influence of dislocation density on the ductile-briitle transition in bcc metals. Scripta Metallurgica 19, 557–562.

Beltz, G.E., Rice, J.R., Shih, C.F., Xia, L., 1996. A self-consistent model for cleavage in the presence of plastic flow. Acta Materialia 44, 3943–3954.

Carreño-Morelli, E., Ghilarducci, A.A., Urreta, S.E., 1999. Dislocation pinning in a low-dose neutron irradiated Al-Mg-Si industrial alloy. Philosophical Magazine A79, 293–304.

Cleveringa, H.H.M., Van der Giessen, E., Needleman, A., 1999a. A discrete dislocation analysis of bending. International Journal of Plasticity 15, 837–868.

Cleveringa, H.H.M., Van der Giessen, E., Needleman, A., 1999b. Discrete dislocations interacting with a mode I crack. Materials Research Symposium Proceedings 538, 39–50.

Cuitiño, A.M., Ortiz, M., 1992. Computational modelling of single crystals. Modelling and Simulation in Materials Science Engineering 1, 225–263.

De Guzman, M.S., Neubauer, G., Flinn, P., Nix, W.D., 1993. The role of indentation depth

on the measured hardness of materials. Materials Research Symposium Proceedings 308, 613–618.

Fleck, N.A., Hutchinson, J.W., 1993. A phenomenological theory for strain gradient effects in plasticity. Journal of the Mechanics and Physics of Solids 41, 1825–1857.

Fleck, N.A., Hutchinson, J.W., 1997. Strain gradient plasticity. Advances in Applied Mechanics 33, 295–361.

Fleck, N.A., Muller, G.M., Ashby, M.F., Hutchinson, J.W., 1994. Strain gradient plasticity: theory and experiment. Acta Metallurgica et Materialia 42, 475–487.

Freund, L.B., 1994. The mechanics of dislocations in strained-layer semiconductor-materials. Advances in Applied Mechanics 30, 1–66.

Freund, L.B., 1998. Dynamic Fracture Mechanics. Cambridge University Press, Cambridge.

Gumbsch, P., Riedle, J., Hartmaier, A., Fischmeister, H.F., 1998. Controlling factors for the brittle-to-ductile transition in tungsten single crystals. Science 282, 1293–1295.

Hirsch, P.B., Roberts, S.G., 1989. The dynamics of edge dislocation generation along a plane orthogonal to a mode-I crack. Scripta Metallurgica 23, 925–930.

Irwin, G.R., 1958. Fracture. In: Flügge, S. (Ed.), Encyclopedia of Physics, vol. VI. Springer–Verlag, New York, pp. 551–590.

Kubin, L.P., Canova, G., Condat, M., Devincre, B., Pontikis, V., Bréchet, Y., 1992. Dislocation microstructures and plastic flow: a 3D simulation. Solid State Phenomena 23/24, 455–472.

Lin, I.-H., Thomson, R., 1986. Cleavage, dislocation emission, and shielding for cracks under general loading. Acta Metallurgica 34, 187–206.

Ma, Q., Clarke, D.R., 1995. Size dependent hardness of silver single crystals. Journal of Materials Research 10, 853–863.

Muskhelishvili, N.I., 1953. Some Basic Problems of the Mathematical Theory of Elasticity. Noordhoff, Leiden.

Needleman, A., 1987. A continuum model for void nucleation by inclusion debonding. Journal of Applied Mechanics 54, 525–531.

Needleman, A., 1990. An analysis of tensile decohesion along an interface. Journal of Solids of the Mechanics and Physics 38, 289–324.

Nitzsche, V.R., Hsia, K.J., 1994. Modeling of dislocation mobility controlled brittle-to-ductile transition. Materials Science and Engineering A 176, 155–164.

Rice, J.R., 1968. A path independent integral and the approximate analysis of strain concentration by notches, cracks. Journal of Applied Mechanics 35, 379–386.

Rice, J.R., 1987. Tensile crack tip fields in elastic-ideally plastic crystals. Mechanics of Materials 6, 317–335.

Rose, J.H., Ferrante, J., Smith, J., 1981. Universal binding energy curves for metals and bimetallic interfaces. Physical Review Letters 47, 675–678.

Shastry, V., Anderson, P.M., Thomson, R., 1994. Nonlocal effects of existing dislocations on crack-tip emission and cleavage. Journal of Materials Research 9, 1–16.

Suo, Z., Shih, C.F., Varias, A.G., 1993. A theory for cleavage cracking in the presence of plastic flow. Acta Metallurgica et Materialia 41, 1551–1557.

Tvergaard, V., Hutchinson, J.W., 1992. The relation between crack growth resistance and fracture process parameters in elastic–plastic solids. Journal of the Mechanics and Physics of Solids 40, 1377–1397.

Van der Giessen, E., Needleman, A., 1995. Discrete dislocation plasticity: a simple planar model. Modelling and Simulation in Materials Science and Engineering 3, 689–735.

Weertman, J., Lin, I.H., Thomson, R., 1983. Double slip plane crack model. Acta Metallurgica 31, 473–482.

Wei, Y., Hutchinson, J.W., 1997. Steady-state crack growth and the work of fracture for solids characterized by strain gradient plasticity. Journal Solids of the Mechanics and Physics of Solids 45, 1253–1273.

Zacharopoulos, N., Srolovitz, D.J., LeSar, R., 1997. Dynamic simulation of dislocation microstructures in mode III cracking. Acta Materialia 45, 3745–3763.